대향 부연소실이 있는 밀폐연소실 내의 NO_X 저감기구에 대한 연구

김 재 헌*, 이 수 갑*, 정 인 석*

A Study on NOx Reduction Mechanism in a Closed Vessel with Opposed Dual Pre-chambers

Jaeheon Kim*, Soogab Lee* and In-Seuck Jeung*

Key words: NO_x, impinging-jet-flame combustion, opposed dual pre-chambers, ignition delay, orifice diameter, spatial distribution of temperature

Abstract

It is well known that NOx formation has a strong dependence on the maximum temperature and correspondingly with the maximum chamber pressure of a closed combustion system. However, in a case of impinging-jet-flame (IJF hereafter) combustion with opposed dual pre-chambers, low NO_x formation with high pressure could be achieved, but its mechanism has not been clearly understood so far. In this study, a three-dimensional analysis is adopted to resolve time-variant local properties that might indicate the mechanism of IJF combustion. Numerical results are verified by comparing them with experiments. The IJF combustion in a vessel with no pre-chamber, with single pre-chamber, and with dual pre-chambers is studied. The orifice diameter and the volumetric ratio of pre-chamber are used as geometric parameters. The effects of main-chamber ignition delay time and combustion time of main-chamber, orifice exit velocity, orifice exit temperature, turbulent kinetic energy of main-chamber and spatial distribution of temperature in the latter stage of combustion are investigated. A longer main-chamber ignition delay and a shorter main-chamber combustion time suppress the formation of high temperature region with respect to mean temperature, which consequently results in less NO production.

1. Introduction

Nitrogen oxide is one of combustion products that contribute to air pollution such as photochemical smog, acid rain, destruction of ozone, global warming, etc. Over the past decades, regulations confining the allowable NO_x emissions have been more and more stringent. Therefore recently developed combustion devices have to satisfy lower NO_x emission regulation as well as higher combustion efficiency.

It is well known that NO_x formation is strongly dependent on the maximum temperature or correspondingly on the maximum chamber pressure of a closed combustion system. But under certain

* Member, Department of Aerospace Engineering, Seoul National University

Nomenclature

English

a, b : Empirical constants used in reaction rate equation
c : Constant used in k-ε turbulence model
D : Diffusion coefficient
h_m : Specific enthalpy for species m
I : Specific internal energy, exclusive of chemical energy
$\bar{\mathbf{I}}$: Unit dyadic
$\mathbf{J}$: Heat flux vector
k : Turbulent kinetic energy or reaction coefficient
m : Mass
p : Fluid pressure
Pr : Prandtl number
$\dot{Q}^c$: Rate of chemical heat release
$\mathbf{u}$: Fluid velocity vector
T : Temperature
t : Time

Greeks

ε : Dissipation rate
λ : Second viscosity coefficient
μ : First viscosity coefficient
ρ : Total mass density
ρ_m : Mass density for species m
$\dot{\rho}_m^c$: Chemical source term
$\bar{\sigma}$: Viscous stress tensor
$\dot{\omega}$: Reaction rate

Subscripts

i : Each spatial point
k : Associated with the turbulent kinetic energy
m : Chemical species
ε : Associated with the dissipation rate
fr : Forward reaction
br : Backward reaction

Superscripts

c : Chemistry or corrected

circumstances, exceptional experimental results have been reported. High chamber pressure and low NO_x can be found in the combustion system using impinging jet/spray flame methods [1,2,3,4]. This might be due to a certain kind of mixing process by intense turbulence. But its mechanism has not been clearly explained yet, because of some practical limits in the previous measurements. So far in experiments, measurement of NO_x concentration was possible only at the post-combustion stage. Furthermore, total NO_x quantity was measured without any information of the local distributions of time-varying properties in the combustion chamber since they could not be easily probed.

In this study, to overcome the limitation of experiments, a numerical approach is employed, which is able to provide detailed temporal and spatial information as well as averaged mean properties.

2. Numerical analysis

It is very difficult to carry out a direct analysis of three dimensional unsteady combustion phenomena in a real combustion chamber. Hence two types of simplified analysis have been selected. One is a zero-dimensional analysis to simulate the variation of chemical species at a fixed point in the combustion chamber while the flame passing the point. The other is a one-dimensional analysis to resolve the spatial change of thermodynamic properties before and behind the flame sheet. Through the simplification in numerical treatments, 82 propane reactions and 5 Zel'dovich thermal NO reactions including 34 chemical species are allowable.[5,6]

From these simplified analyses, only the common

characteristics of NO formation are simulated and it is found that the mechanism of NO reduction in IJF combustion with opposed dual pre-chambers can not be explained by the simplified zero- or one-dimensional analysis. From this reason, three-dimensional analysis is performed to resolve local time-varying physical properties.

2.1 Governing Equations

The numerical solutions are obtained by a modified version of KIVA-II[7]. Governing equations include $k-\varepsilon$ turbulence model to treat turbulent flow field, and involve one-step global oxidization reaction, three thermal NO reactions, and six equilibrium reactions so to deal with propane reaction.

2.1.1 Continuity equation

The continuity equation for species m is

$$\frac{\partial \rho_m}{\partial t} + \nabla \cdot (\rho_m \mathbf{u}) = \nabla \cdot \left[\rho D \nabla \left(\frac{\rho_m}{\rho} \right) \right] + \dot{\rho}_m^c \tag{1a}$$

Fick's law with a single diffusion coefficient D is assumed. If equation (1a) is summed over all species, the total fluid density equation is obtained as

$$\frac{\partial \rho}{\partial t} + \nabla \cdot (\rho \mathbf{u}) = 0 \tag{1b}$$

2.1.2 Momentum equation

The momentum equation for the fluid mixture is

$$\frac{\partial (\rho \mathbf{u})}{\partial t} + \nabla \cdot (\rho \mathbf{u}\mathbf{u}) = -\frac{1}{a^2} \nabla p - \nabla \left(\frac{2}{3\rho k} \right) + \nabla \cdot \bar{\sigma} \tag{2}$$

The viscous stress tensor is

$$\bar{\sigma} = \mu \left[\nabla \mathbf{u} + (\nabla \mathbf{u})^T \right] + \lambda \nabla \cdot \mathbf{u} \bar{\mathbf{I}} \tag{2a}$$

2.1.3 Energy equation

The energy equation is

$$\frac{\partial (\rho I)}{\partial t} + \nabla \cdot (\rho \mathbf{u} I) = -p \nabla \cdot \mathbf{u} - \nabla \cdot \mathbf{J} + \rho \varepsilon + \dot{Q}_c \tag{3}$$

where the heat flux vector $\mathbf{J}$ is given by

$$\mathbf{J} = -K \nabla T - \rho D \sum_m h_m \nabla (\rho_m / \rho) \tag{3a}$$

2.1.4 k-ε turbulence equations

The standard k-ε equations with some added terms are used:

$$\frac{\partial \rho k}{\partial t} + \nabla \cdot (\rho \mathbf{u} k) = -\frac{2}{3} \rho k \nabla \cdot \mathbf{u} + \bar{\sigma} : \nabla \mathbf{u} + \nabla \cdot \left[\left(\frac{\mu}{\mathrm{Pr}_k} \right) \nabla k \right] - \rho \varepsilon \tag{4a}$$

and

$$\frac{\partial \rho \varepsilon}{\partial t} + \nabla \cdot (\rho \mathbf{u} \varepsilon) = -\left(\frac{2}{3} c_{\varepsilon_1} - c_{\varepsilon_3} \right) \rho \varepsilon \nabla \cdot \mathbf{u} + \nabla \cdot \left[\left(\frac{\mu}{\mathrm{Pr}_\varepsilon} \right) \nabla \varepsilon \right] + \frac{\varepsilon}{k} \left[c_{\varepsilon_1} \bar{\sigma} : \nabla \mathbf{u} - c_{\varepsilon_2} \rho \varepsilon \right] \tag{4b}$$

The quantities c_{ε_1}, c_{ε_2}, c_{ε_3}, Pr_k, and Pr_ε are constants whose values are determined from experiments and some theoretical considerations. Standard values of these constants are c_{ε_1}=1.44, c_{ε_2}=1.92, c_{ε_3}=-1.0, Pr_k=1.0, and Pr_ε=1.3.

2.2 Chemical Reaction Equations

Chemical reactions are calculated by one-step global oxidization equation, three thermal NO reactions, and six equilibrium equations.

2.2.1 One-step global oxidization equation

The global oxidization reaction of propane becomes

$$C_3H_8 + 5(O_2 + 3.76N_2) \rightarrow 3CO_2 + 4H_2O + 18.8N_2 \tag{5}$$

2.2.2 Three thermal NO reactions

$$O_2 + 2N_2 \rightleftarrows 2NO + 2N \tag{6a}$$

$$N_2 + 2O_2 \rightleftarrows 2NO + 2O \tag{6b}$$

$$2OH + N_2 \rightleftarrows 2NO + 2H \tag{6c}$$

The reaction rates of the global oxidization equation and thermal NO reactions are given by

$$\dot{\omega}_r = k_{fr}\prod_m\left(\frac{\rho_m}{W_m}\right)^{a'_{mr}} - k_{br}\prod_m\left(\frac{\rho_m}{W_m}\right)^{b'_{mr}} \quad (7)$$

Here the reaction orders a'_{mr} and b'_{mr} are empirical ones, and the coefficients k_{fr} and k_{br} are assumed to be of a generalized Arrhenius form.

$$k_{fr} = A_{fr}T^{\zeta_r}\exp\left(-E_{fr}/RT\right) \quad (7a)$$

$$k_{br} = A_{br}T^{\zeta_r}\exp\left(-E_{br}/RT\right) \quad (7b)$$

where E_{fr} and E_{br} are activation temperatures. Table 1 gives the coefficients used in the above reactions.

2.2.3 Six equilibrium reactions

$$H_2 \underset{\leftarrow}{\rightarrow} 2H \quad (8a)$$

$$O_2 \underset{\leftarrow}{\rightarrow} 2O \quad (8b)$$

$$N_2 \underset{\leftarrow}{\rightarrow} 2N \quad (8c)$$

$$O_2 + H_2 \underset{\leftarrow}{\rightarrow} 2OH \quad (8d)$$

$$O_2 + 2H_2O \underset{\leftarrow}{\rightarrow} 4OH \quad (8e)$$

$$O_2 + 2CO \underset{\leftarrow}{\rightarrow} 2CO_2 \quad (8f)$$

The rates of the above reactions are given by the following equation;

$$\prod_m\left(\frac{\rho_m}{W_m}\right)^{b_{mr}-a_{mr}} = K_c^r(T) \quad (9)$$

	Reaction	A (mole cm^3 sec)	ζ	E (kJ/mole)
1	$O_2 + 2N_2 \rightarrow 2NO + 2N$	1.5587×10^{14}	0	561.98
2	$O_2 + 2N_2 \leftarrow 2NO + 2N$	7.5000×10^{12}	0	0.0
3	$N_2 + 2O_2 \rightarrow 2NO + 2O$	2.6484×10^{10}	1.0	493.76
4	$N_2 + 2O_2 \leftarrow 2NO + 2O$	1.6000×10^{9}	1.0	163.52
5	$N_2 + 2OH \rightarrow 2H + 2NO$	2.1230×10^{14}	0	473.84
6	$N_2 + 2OH \leftarrow 2H + 2NO$	0.0	0	0

Table 1 Coefficients of NO kinetic reactions

Reactions	A	B	C	D	E
$H_2 \underset{\leftarrow}{\rightarrow} 2H$	0.990207	-51.7916	0.99307	-0.343428	0.0111668
$O_2 \underset{\leftarrow}{\rightarrow} 2O$	0.431310	-59.6554	3.50335	-0.340016	0.0158715
$O_2 + H_2 \underset{\leftarrow}{\rightarrow} 2OH$	0.794709	-113.2608	3.16837	-0.340016	0.0269697
$O_2 + H_2 \underset{\leftarrow}{\rightarrow} 2OH$	-0.652939	-9.8232	3.93033	0.163490	-0.014286
$O_2 + 2H_2O \underset{\leftarrow}{\rightarrow} 4OH$	0.158882	-76.8472	8.53215	-0.868320	0.0463471
$O_2 + 2CO \underset{\leftarrow}{\rightarrow} 2CO_2$	0.980875	68.4453	-10.59380	0.574260	-0.0414570

Table 2 Coefficients of equilibrium reactions

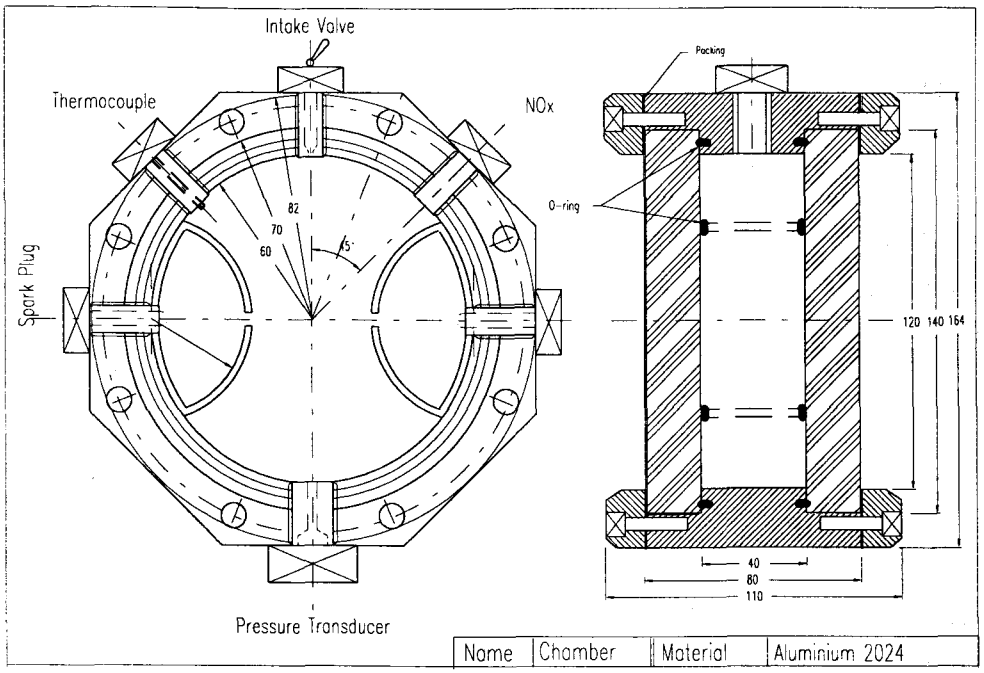

Fig 2.1 Combustion vessel with opposed dual pre-chambers used in experimental study; total volume = 452cc, V_p/V_t = 14.8%, diameter of vessel =120mm, height = 40mm

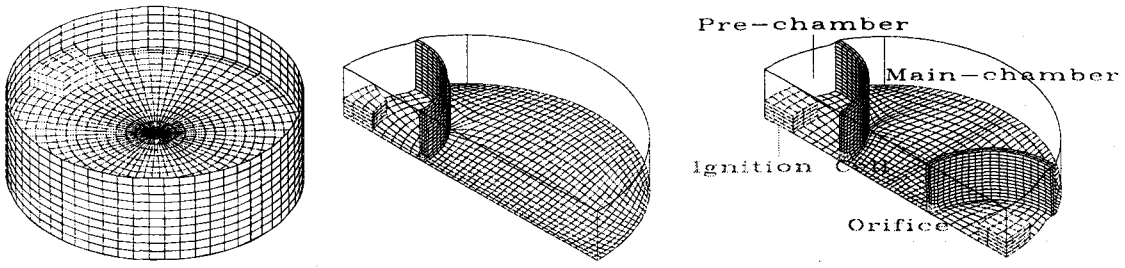

(a) (b) (c)

Fig 2.2 Grid system used in numerical calculation;
(a) discal vessel with no pre-chamber, (b) with single pre-chamber, (c) with dual pre-chambers

where the density equilibrium coefficient $K_c^r(T)$ is

$$K_c^r(T) = \exp\left[A_r \ln T_A + \frac{B_r}{T_A} + C_r + D_r T_A + E_r T_A^2 \right]$$
$$where \quad T_A = T/1000\,(K) \tag{9a}$$

Table 2 gives the reaction coefficients of the equilibrium equations.

The details of these simplified chemical reactions can be found in references[7, 8]. In three-dimensional analysis, the above simplified chemical reactions are used due to the limitation of computer capacity, although 82 propane reactions and 5 thermal NO reactions are allowable in zero- or one-dimensional analysis.

2.3 Grid Generation and β Transformation

Computational grid system is generated with the geometry of the flat discal combustion chamber (Fig

2.1) used in the experimental studies of our laboratory.[4]

Three types of grid system are used for numerical calculation; [1] a discal chamber with no pre-chamber, [2] one with single pre-chamber, and [3] one with dual pre-chambers (Fig 2.2). The dual pre-chambers type vessel is the main object of this study, and it is generated with variations of the shape of pre-chamber, the volumetric ratio of pre-chamber to total vessel, and the orifice diameter of pre-chamber. When the vessel with single or dual pre-chambers is analyzed, only a quarter of total combustion chamber is simulated due to symmetry.

Since a typical flame thickness of hydrocarbon is order of 0.01 cm, it is almost impossible to resolve this thin flame zone by simply using the above grid system. Of course, a highly dense grid system can be adopted to settle this problem, but computer capacity will be the point at issue. Introducing β transformation method brings these problems to settlement. The β transformation method[9] is an artificial flame-enlarging method without change of burning velocity and flow characteristics. While all transport properties are multiplied by β, the chemical reaction rate is divided by β. The heat generated by flame surface is still equivalent with that of the case without using β transformation method. The value of β is determined by

$$\beta(T) = \mathrm{Max}\left(1, \frac{C\Delta x^2}{\delta}\frac{|\nabla T|}{\Delta T}\right) \qquad (10)$$

where $C = 4\,cm$, $\delta = 0.02\,cm$, $\Delta T = 2000\,K$.

2.4 Initial and Boundary Conditions

A propane-air premixed gas of 3.8% volumetric mixture ratio is used. This premixed gas is initially charged into the combustion chamber at atmospheric pressure (1 atm) and room temperature (300K). Energy deposits simulate spark ignition. That is to say, total internal energy in the specified ignition cells is forced to increase by a factor of (1.0 + 5000ergs/g/s × discrete time step) until the temperature of the ignition cells reaches 1200K at which a self-ignition occurs. The law-of-wall condition is used as a velocity boundary condition. The fixed wall temperature of 300K is used as a wall boundary condition with no chemical reaction at the wall. Laminar Prandtl number is assumed to be 0.74 over all processes.

3. Results and Discussion

Generally speaking, an increase in maximum pressure results in higher NO production. This general rule applies well in cases of both non and a single pre-chamber case. But, surprisingly it is not true in cases of dual opposed pre-chambers: Depending on the diameter of the orifice, NO production is observed to actually decrease with maximum pressure increase (Fig 3.1). In Fig 3.1, the numerical results of NO concentration with maximum chamber pressure are plotted in comparison with experiments. The numerical results have a similar tendency with experimental ones. But the numerical values have higher maximum pressure than those of experiments due to heat loss to the wall, which is not fully considered in the numerical calculation. Fig 3.2 shows temperature contours in the combustion chamber, comparing numerical results with experiments of Jeung[4]. The volumetric ratio of pre-chamber to total chamber is 14.8% and the orifice size of pre-chamber is 5mm. It is shown that numerical results make a good reproduction of real phenomena.

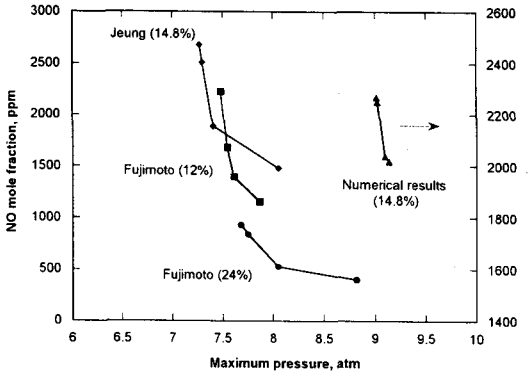

Fig 3.1 Relation between NO concentration and maximum chamber pressure with varying orifice diameter

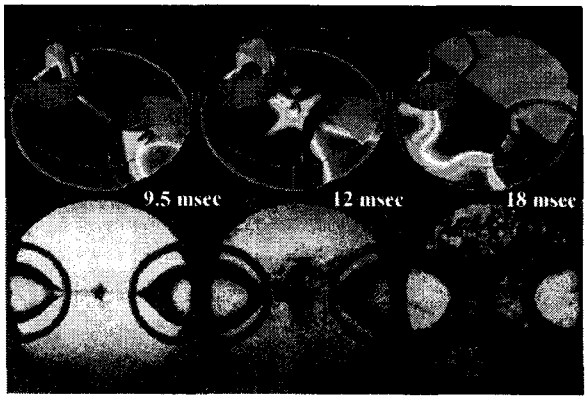

Fig 3.2 Temperature contours and Schlieren photos : orifice diameter = 5mm

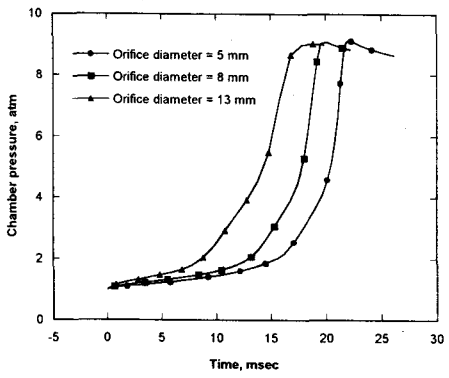

Fig 3.3 Pressure-time traces with varying orifice diameter of dual pre-chambers: V_p/V_t = 14.8% of dual pre-chambers; Fujimoto, Jeung : experiment

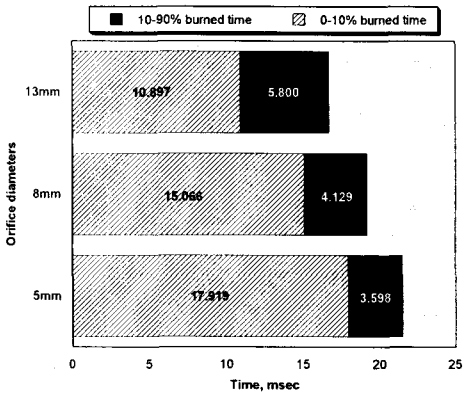

Fig 3.4 Comparison of burning time for each orifice diameter (0-10% burned and 10-90% burned)

3.1 Ignition delay of main-chamber combustion

Fig 3.3 illustrates the time variations of averaged main-chamber pressure. This figure reveals that in case of pre-chamber with a equal volumetric ratio of 14.8%, the decrease of the orifice size results in slightly higher maximum pressure, with a longer time to reach the maximum pressure. Time delay between the pre-chamber ignition and main-chamber ignition (MCI hereafter) is also shown in this figure.

Fig 3.4 illustrates MCI delay time and combustion time of main-chamber with a variation of orifice diameter. The combustion processes are divided to 0 to 10 and 10 to 90% propane mass fraction burned times. The former is regarded as MCI delay time and the latter as main-chamber combustion time. The total time of 0 to 90% burned is shorter for a smaller orifice diameter. This figure shows a trend of an increase in the 0 to 10% burned time and a decrease in the 10 to 90% burned time with a smaller orifice size. Fig 3.5 relates the NO production, maximum chamber pressure, and 10-90% burned time to 0-10% burned time. As the MCI delay time, i.e. 0 to 10% burned time, is increased by reducing orifice size, the

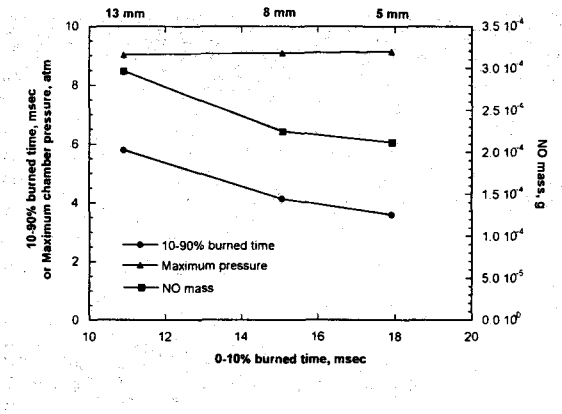

Fig 3.5 10-90% burned time, NO production, and maximum chamber pressure for 0-10% burned time

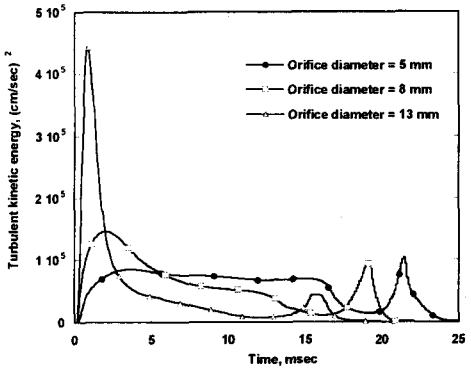

Fig 3.6 Turbulent kinetic energy of main-chamber as a function of time; V_p/V_t = 14.8%

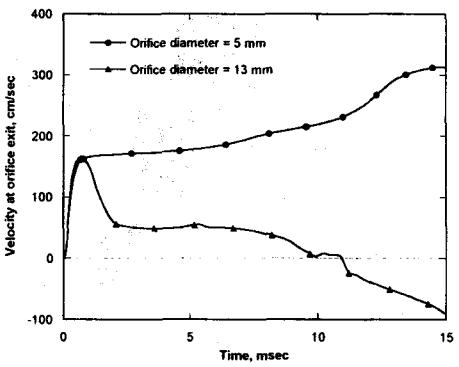

Fig 3.7 Mean velocity history at orifice exit of dual pre-chambers; V_p/V_t = 14.8%; 5 and 13mm orifice

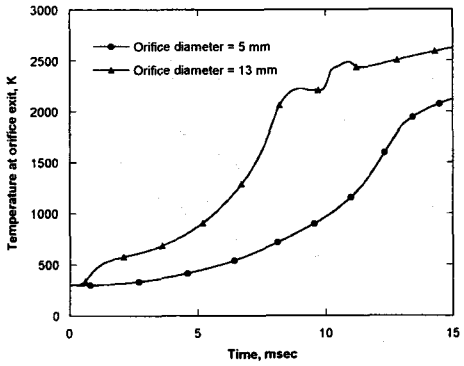

Fig 3.8 Mean temperature history at orifice exit of dual pre-chambers; V_p/V_t = 14.8%

NO production declines due to reduction in main-chamber combustion time, while maximum pressure is maintained throughout. Reduction in main-chamber combustion time reduces NO production by decreasing exposure time to high temperature and pressure while efficient combustion is executed with minimum heat loss.

3.2 Flow characteristics related to MCI delay

As shown above, the MCI delay is closely related to NO production, and a thorough investigation of parameters causing the delay is thus necessary. So, the flow characteristics until MCI time are investigated.

Fig 3.6 illustrates turbulent kinetic energy of main-chamber as a function of time. For a larger orifice size, more turbulent kinetic energy is concentrated on the initial stage and rapidly diminishes with time, whereas an even time distribution of turbulent kinetic energy occurs for a smaller orifice size. In the initial stage, turbulence is dominantly caused by the ejection from pre-chambers. MCI occurs when the turbulent

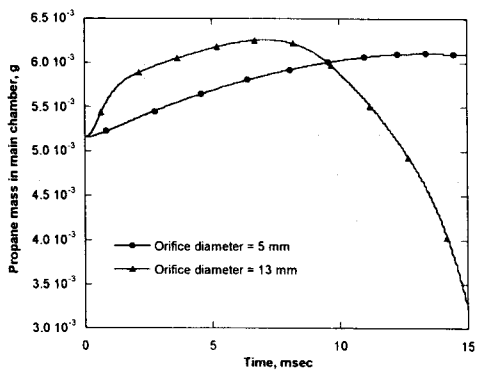

Fig 3.9 Variations of propane mass in main-chamber as a function of time; V_p/V_t = 14.8%

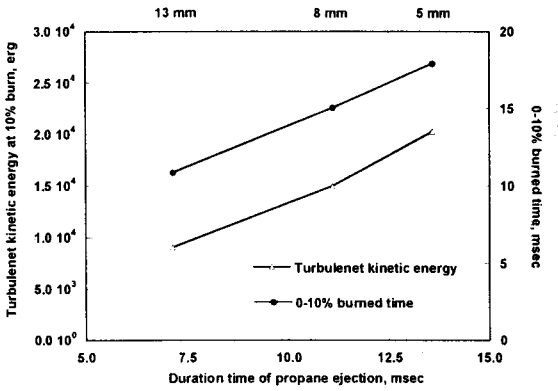

Fig 3.10 Duration time of propane ejection with 0-10% burned time and turbulent kinetic energy at 10% propane mass fraction burn

kinetic energy is somewhat reduced, and in the final stage, turbulent kinetic energy is increased again by combustion. The ejected flow from pre-chambers is characterized by the orifice exit velocity pattern, which is shown in Fig 3.7. In this figure, the cases with orifice sizes of 5mm and 13mm are compared. For the 5mm orifice diameter, the ejection flow from orifice lasts longer than the case of the 13mm orifice diameter. Interestingly, a reverse flow to the pre-chamber from the main-chamber in the latter stage is shown in case of 13mm orifice diameter. Fig 3.6 and Fig 3.7 imply that the initial turbulent flow pattern of main-chamber is directly affected by the orifice exit flow.

Fig 3.8 represents temperature histories at orifice exit, illustrating that a smaller orifice keeps a lower temperature than the self-ignition point for a longer time. Fig 3.9 confirms this fact by illustrating the variations of propane mass in main-chamber as a function of time. For a smaller orifice size, increase of propane mass in main-chamber caused by ejected unburned mixture from pre-chamber is maintained for a longer time. Summing up, the MCI delay is strongly influenced by relatively cold turbulent flow driven by initial ejection containing unburned mixture from pre-chambers. Fig 3.10 makes this relation clear by representing the ejection duration of propane from pre-chamber with 0-10% burned time and turbulent kinetic energy at 10% burned point, where the ejection duration of propane is defined as time consumed to reach the maximum propane mass in main-chamber.

3.3 Spatial distribution of temperature

NO is particularly sensitive to temperature, and consequently most of NO is produced in the high temperature region in the latter stage of combustion. To analyze this effect, a new concept representing the local distribution of temperature is introduced. Mass Weighted Standard Deviation (MWSD hereafter) of temperature is defined as follows.

$$MWSD = \left(\frac{\sum_i m_i \left(T_i - T_{avg} \right)^2}{\sum_i m_i T_{avg}^2} \right)^{1/2} \qquad (11)$$

where m_i is local mass of each point, T_i is local

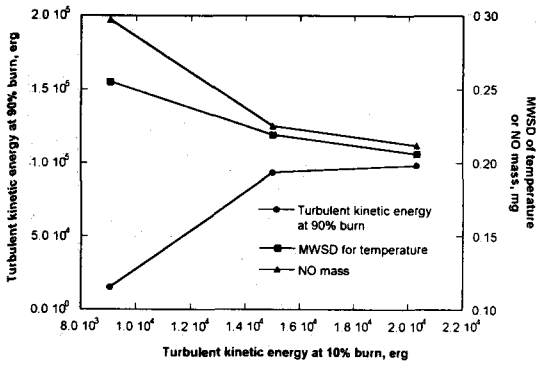

Fig 3.11 Turbulent kinetic energy, MWSD for temperature at 90% burn, and NO mass at 90% burn as a function of turbulent kinetic energy at 10% burn

temperature, and T_{avg} is mean temperature. MWSD physically represents the mixing effectiveness of the flow field in combustion chamber.

To investigate the effect of flow characteristics prior to MCI on latter parts of combustion, the relationship of turbulent kinetic energy, MWSD, and NO mass at 90% burn to turbulent kinetic energy at 10% burn is illustrated in Fig 3.11. Larger initial turbulent kinetic energy results in larger turbulent kinetic energy and lower MWSD distribution, and lower NO mass in the latter stages of combustion. A small value of MWSD of temperature implies a well-mixed temperature distribution, i.e. a distribution centered near the mean value. The above also implies that higher temperature regions with respect to mean temperature is suppressed and NO production depending on high temperature region is decreased.

4. Conclusions

Numerical calculations have been done mainly for the combustion vessel with dual opposed pre-chambers (opposed IJF combustion). To verify the results from numerical analysis, they are compared with experiments and both results have a similar tendency with each other. Observation of time distribution of main-chamber pressure and fuel mass fraction reveals that, in case of dual pre-chambers with a volumetric ratio of 14.8%, decreasing of orifice size results in longer MCI delay time. For a longer MCI delay time, NO production is declined due to reduction in main-chamber combustion time, while maximum pressure is maintained throughout.

To seek the parameters affecting MCI delay and main-chamber combustion time reduction, various investigations of main-chamber flow field as well as orifice exit flow characteristics are performed. The strong turbulence field generated by ejection flow containing unburned mixture from pre-chamber prior to ignition in the main-chamber has been found to have considerable effect on MCI delay. The initial turbulent flow also considerably influences the spatial temperature distribution in the latter parts of main-chamber combustion. A longer MCI delay induces a shorter main-chamber combustion time and suppresses the formation of high temperature region with respect to mean temperature, which consequently results in less NO production.

5. Acknowledgment

This work was financially supported by System Engineering Research Institute - Cray R&D program in 1996.

6. References

1 Miura, S., Tsukamoto, T., Kawagoe, M., Nakaoji, S., and Kaneko, Y., "NOx Formation with Various Combustion Processes of Premixed Gas", Mitsubishi Heavy Industries, Technical Review, pp.1-12, 1979

2 Fujimoto, S., Kaneko, Y., and Tsuruno, S., "Possibility of Low-NOx and High-Load Combustion in Premixed Gases", Twentieth Symposium (International) on Combustion, The Combustion Institute, pp.61-66, 1984

3 Okajima, S., and Kumagai, S., "Experimental Investigation of Soot and NOx Reduction by Impinging Spray Combustion in a Closed Vessel", Twenty-third Symposium (International) on Combustion, The Combustion Institute, pp.275-279, 1990

4 Jeung, I.S., and Cho, K.K., "Experimental Study of NOx Reduction by Impinging-Jet-Flame in a Closed Vessel with Opposed Dual Prechambers", in Carvalho M.G. et al (Ed.) Combustion Technologies for a Clean Environment, Gordon and Breach Science Publisher, in press

5 Peters, N., Rogg, B., "Reduced Kinetic Mechanism for Applications in Combustion System", Springer-Verlag, 1993

6 Glarborg, P., Miller, J.A., and Kee, R.J., "Kinetic Modelling and Sensitivity Analysis of Nitrogen Oxide Formation in Well-stirred Reactors", Combustion and Flame, vol. 65, pp.177-202, 1986

7 Amsden, A.A., O'Rourke, P.J., and Butler, T.D., "KIVA-II: A Computer Program for Chemically Reactive Flows with Sprays", Los Alamos Scientific Laboratory Report, 1989

8 Westbrook, C.K., and Chase, L.L., "Chemical Kinetics and Thermodynamical Data for Combustion Application", Lawrence Livermore Laboratory, 1983

9 Butler, T.D., and O'Rourke, P.J., "A Numerical Method for Two Dimensional Unsteady Reacting Flows", Sixteenth Symposium (International) on Combustion, pp.1503-1515, 1976